

Analysis of Newly Catalogued Open Star Cluster UPK 220 with Gaia DR3 and TESS: Discovering Member Variable Stars

İNÇİ AKKAYA ORALHAN ^{1,2}, CENK KAYHAN ³ AND ÖZGÜN ARSLAN ^{1,2}

¹*Department of Astronomy and Space Sciences,
Science Faculty, Erciyes University,
38030 Melikgazi, Kayseri, Türkiye*

²*Astronomy and Space Sciences Observatory and Research Center (Uzaybimer),
Erciyes University, 38281, Talas, Kayseri, Türkiye*

³*Scientific Research Projects Coordination Unit,
Kayseri University,
38280, Talas, Kayseri, Türkiye*

ABSTRACT

Studies on star clusters with the same age and initial chemical composition have gained momentum in recent years with the use of *Gaia*. In addition, the discovery of new clusters with *Gaia* has increased the number of open clusters to be examined. Many of these discovered sources are intermediate-age open clusters and have not been analyzed in detail yet. In this study, we focused on newly cataloged open cluster UPK 220. The fundamental parameters (distance, age, metallicity and reddening) of UPK 220 were determined by analysing the variable stars within the cluster, while simultaneously constraining the parameters of the variable stars using these cluster parameters. To achieve this, we combined GaiaDR3 and TESS photometric observations. Using GaiaDR3, we derive fundamental parameters of UPK 220 through membership analyses, and with TESS, we discovered eight member variable stars. We also extracted the atmospheric parameters ($\log g$, $[Fe/H]$ and T_{eff}) for the variable stars using SED, GSP-Phot and GSP-Spec, and MESA models.

Keywords: Open clusters(1160) — Stellar Photometry(1234) — Gaia(2360) — Variable stars(1761) — Stellar Evolution(1599)

1. INTRODUCTION

Open clusters (OCs) are gravitationally bound stellar populations, which show characteristic number density profiles of member stars with respect to field stars (King 1966; Krumholz et al. 2019; Sariya et al. 2023). According to their ages, OCs can be classified into three main categories: young ($< 10^6$ yr), intermediate-age ($10^6 - 10^7$ yr) and old ($> 10^7$ yr) (Friel 1995; Im et al. 2023).

OCs may involve a few hundred to thousand member stars depending on the initial physical conditions of the molecular cloud regions where they formed and their galactic location within the Galactic disc. Therefore, OCs are paradigmatic coeval systems to investigate the

formation of stars and stellar evolution but also critically important to understand the chemical and dynamical structure within the Galactic disc (Barnes 2007; Kim et al. 2017; Cantat-Gaudin et al. 2018; Cantat-Gaudin et al. 2020).

The predicted total number of galactic OCs is near of 10^5 (Piskunov et al. 2006). For this reason, many extensive studies have been carried out to identify candidate OCs, as well as to comprise advance catalogs of OCs based on multiple photometric surveys (Mermilliod 1981; Dias et al. 2002; Cutri et al. 2003; Kharchenko et al. 2005, 2013). However, the number of known OCs within available catalogs produced before the *Gaia* Mission (Prusti et al. 2016) is substantially restricted due to photometric limits, field star contamination, spatial resolution, and dust extinction (He et al. 2022b; Chi et al. 2023).

The census of discovered OCs dramatically increased with the Gaia Data Release 2 (hereafter GaiaDR2) (Cantat-Gaudin et al. 2018; Soubiran et al. 2018; Liu & Pang 2019; Castro Ginard et al. 2020; Monteiro et al. 2020). Considering certain astrometric and photometric data such as equatorial coordinates (α, δ), proper motions (μ_α, μ_δ), trigonometric parallaxes (ϖ), and magnitudes (the white-light G, the blue G_{BP} , and the red G_{RP}) with the accompanied errors, the effective separation between member stars and field stars across an OC region can be achieved (Uribe et al. 2002; Gao 2018). Gaia Data Release 3 (Gaia Collaboration et al. 2023, hereafter GaiaDR3), an updated version of GaiaDR2, provides quite a suitable and homogeneous data set to investigate and promote the fundamental parameters of Galactic OCs (He et al. 2022a). The database comprises nearly 1.8 billion celestial objects with magnitudes up to 19th in the G band, presenting fairly homogeneous and low photometric uncertainties (Negueruela & de Burgos 2023). Therefore, GaiaDR3 gives us an ideal data set to study high-precision photometric analyses of OCs and the parameters of a cluster can be determined with greater precision (Lada & Lada 2003; Yadav et al. 2011; Ahumada et al. 2013; Pietrzyński et al. 2019; Castro Ginard et al. 2020).

The mass distribution of OC members result in the stars undergoing disparate evolutionary stages despite their identical age (Bonatto & Bica 2005; Bonatto et al. 2006). In addition to the evolutionary stages observed, some members have been identified as variable stars. These variable member stars are classified mainly into two subtypes that are based on intrinsic and extrinsic variations (Xin et al. 2002; Mowlavi et al. 2013; Chehlaeh et al. 2018; Dar et al. 2018; Jiang 2020; Kharchenko et al. 2022; Wang et al. 2022a; Zhuo et al. 2021).

Studying variable stars in an OC will bring constraints to the determination of both parameters of the cluster and variable member stars. In this way, the physical parameters of the cluster, such as distance (d), age (t), metallicity ($[Fe/H]$), and interstellar reddening ($E(G_{BP} - G_{RP})$) that is determined from GaiaDR3 data, are used as input parameters in constructing the models of the variable stars. Thus, the model parameters of these discovered variable stars will be determined more precisely (Durgapal et al. 2020; Shen et al. 2021).

In this study, the variable member stars detected by Transiting Exoplanet Survey Satellite (hereafter TESS, Ricker et al. 2014, 2015) photometric observations. TESS is a crucial telescope for the detection of variable stars. TESS possesses comprehensive sky scanning capabilities and high temporal resolution, with two dis-

tinct cadences: short (120 sec) and long (30 min) (Sun et al. 2022).

The majority of OC studies focus on the fundamental parameters of the cluster, with relatively little emphasis on individual members or the influence of those overall cluster properties. However, there are several studies in which both cluster membership analyses are conducted and the parameters of the member variable stars are compared with the cluster fundamental parameters (e.g. Bedding et al. (2023); Frasca et al. (2023); Lata et al. (2023); Fritzewski et al. (2024)). It is therefore important to perform studies that make such comparisons while integrating data from different databases. These efforts enhance the sensitivity of parameter determinations for both the cluster and its members. Moreover, members of OCs may include photometric or spectroscopic variable stars. In such cases, the variable stars within OC members may serve to reduce uncertainties in the fundamental parameters of the cluster, given the fact that they share the same age and initial chemical composition.

In this study, the most up-to-date database, GaiaDR3, is employed for the high-precision analysis of cluster membership. Additionally, TESS observations are utilized to identify photometric variable stars in the studied cluster UPK 220. UPK 220 is a newly discovered intermediate-age OC included in the Ulsan Pusan Korea (UPK) star cluster catalog. The UPK catalog exemplifies the efficiency of GaiaDR2 in detecting new OCs within the Galactic disc (Sim et al. 2019). UPK 220 is located in the second Galactic quadrant at a distance of 967 pc, with an estimated age of 560 Myr (Sim et al. 2019). Its central equatorial coordinates $\alpha_{J2000} = 23^h 23^m 46.1^s$, $\delta_{J2000} = +66^\circ 30' 18''$ are recently estimated by Tarricq et al. (2021). Its astrophysical parameters have not been comprehensively revised, and discrepancies in its estimated t , d , and $[Fe/H]$ have been reported in the literature (Cantat-Gaudin et al. 2020; Cavallo et al. 2023; Alfonso et al. 2024).

This paper is organized as follows: the membership selection and member variability are presented in Section 2. The determination of the cluster parameters and the analysis results of variable stars are presented in Sections 3 and 4. Finally, Discussion and Conclusion are summarized in Sections 5 and 6.

2. DATA AND METHOD

This section outlines the methodology used for the membership analysis of the stars within the cluster region using GaiaDR3 data. It also details the procedures employed to determine whether the members exhibit

variability and to classify their variable types based on photometric variations observed by TESS data.

2.1. Membership Selection

Analyses of the OCs is difficult by the presence of contaminating foreground and background stars in the projected field of view. Therefore, it is essential to distinguish cluster members from field stars using a decontamination algorithm. In this study, we employ the pyUPMASK algorithm, an enhanced version of the original UPMASK algorithm (Pera et al. 2021). Since UPK 220 spans a relatively wide field of view ($\sim 0.5^\circ$) on the sky, the parameters μ_α and μ_δ , ϖ and G , G_{BP} and G_{RP} from GaiaDR3, along with their uncertainties, were extracted for stars within a 30-*arcmin* radius to apply pyUPMASK.

In the proper motion vector diagram of UPK 220 shown in Figure 1 (*upper panel*), we restricted the sample to stars with parallaxes in the range $0.95 \leq \varpi < 1.1$ *mas* based on the distance estimates from Sim et al. (2019). This selection effectively removed many foreground and background stars. The histogram of membership probabilities obtained from pyUPMASK is displayed in Figure 1 (*lower panel*) for 284 stars. Based on these probabilities, we classified stars with a membership probability $P \geq 0.725$ as cluster members, yielding 163 members. The red dashed line in the histogram represents the threshold at which the star counts begin to increase, thereby distinguishing the member stars from field stars. From the member stars, the median parallax and proper motion values for the cluster members were determined to be $\varpi = 1.03 \pm 0.03$ *mas* and $(\mu_\alpha, \mu_\delta) = (-2.41 \pm 0.11, -2.64 \pm 0.12)$ *mas/yr*, respectively. For comparison, Sim et al. (2019) reported proper motion values of $(\mu_\alpha, \mu_\delta) = (-2.41 \pm 0.13, -2.59 \pm 0.12)$ *mas/yr*.

To determine the size of UPK 220, its stellar radial density profile (RDP) was constructed using GaiaDR3 data by counting stars within concentric rings of increasing width centered on the cluster as see in Figure 2. From a King profile fit (King 1966), we derived the central stellar density (σ_{ok}), core radius (R_c) and residual background density (σ_{bg}) for UPK 220. The obtained parameters are $\sigma_{ok} = 0.835 \pm 0.121$ *stars/arcmin*², $R_c = 5.751 \pm 1.079$ *arcmin*, and $\sigma_{bg} = 0.674 \pm 0.023$ *stars/arcmin*². According to the RDP, we adopt the cluster limit radius $R_{lim} = 24.0$ *arcmin* as the outer boundary. Considering King’s profile fitting, we accept 148 stars within UPK 220 limit radius as the probable cluster members.

2.2. Members Variability

UPK 220 is observed by TESS in five different sectors with 30-min (sectors 17, 18 and 24) and 2-min (sec-

tors 57 and 58) cadences. The data that is produced by Science Processing Operations Center (SPOC, Jenkins et al. 2016) is downloaded from Barbara A. Mikulski Archive for Space Telescopes (MAST) database¹. TESS total observed time of member stars UPK 220 is 124.29 days. However, there are two significant gaps in the observation timeline: one between sectors 18-24, and another between sectors 24-57². We analyzed the photometric data of UPK 220 using Full-Frame Image (FFI) obtained by TESS. We used `lightkurve` code (Lightkurve Collaboration et al. 2018) to obtain light curves of UPK 220 members from FFIs. To minimize to contamination from nearby stars, we employed TESS-cut (Brasseur et al. 2019) to extract cutouts of the FFIs for each target. Since the resolution of TESS is limited (1 TESS pixel = ~ 21 *arcsec*, Ricker et al. 2015), we used varying sizes of target and background apertures based on the brightness of the targets. After removing background and other light contributions, we produced light curves of each members. From these light curves, we identified eight member stars exhibiting variability, listed in Table 1. The star IDs correspond to their cluster membership designations. Among these, three stars (IDs 29, 67 and 116) are classified as eclipsing binaries, two stars (IDs 49 and 138) are pulsating, two stars (IDs 16 and 42) are magnetic active, and one star (ID 147) is a rotating variable. Figure 3 further illustrates the positioning of these stars within the boundaries of the cluster.

We computed the Fourier spectrum and their periodogram for the variable stars within a period range of 0.01 to 27 days, corresponding to the observation duration of the TESS sectors. For each variable star, we calculated the signal-to-noise ratio (SNR) of the highest amplitude peak in each frequency spectrum. Periodic variability was considered valid for frequency peaks with an SNR of four or higher, as recommended by Breger et al. (1993). According to their variability, we classified based on the shape of their light curves and their period range.

2.2.1. Eclipsing binary

For eclipsing binaries, we modeled their light curves using v43 version of the JKTEBOP code (Southworth et al. 2004). The code has fast modeling feature by simulating eclipsing binaries. It has also detailed error anal-

¹ <https://mast.stsci.edu/portal/Mashup/Clients/Mast/Portal.html>
² Details can be found in the TESS Data Release Notes (DRN). For Sectors 17, 18, 24, 57 and 58 (DRN 24, 25, 35, 82 and 83, respectively), they are available at https://archive.stsci.edu/tess/tess_drn.html.

ysis including Monte Carlo error analysis algorithms. However, intrinsic variations such as pulsation or stellar spots cannot be included in the light curve models of calculations in the code.

In this study, we modeled light curves of eclipsing binaries IDs 29, 67 and 116, which were obtained from TESS observations in sectors 17, 18, 24, 57 and 58. We also determined $1\text{-}\sigma$ uncertainties using Monte Carlo and residual-permutation simulations. We noticed that there are few data points around the ingress and egress phases in sectors 17, 18, and 24 due to the long cadence mode with a 30-min sampling rate. Since this situation affects the precision of the fractional radii derived from the best-fitting model and could lead to erroneous results. Therefore, the light curves obtained from sectors 57 and 58 observations of TESS (short cadence mode with 120-sec sampling rate) that have more data points around the egress and ingress phases are decisive in the models.

To prepare the data for light curve modeling, data is converted the TESS flux to T_{mag} using Pogson equation. The initial orbital period (P_{orb}) and time of periastron of the primary eclipse (T_p), orbital inclination (i), periastron longitude omega (w), fractional radius of stars (r_A and r_B), orbital eccentricity (e), light ratio (l_B/l_A) are adjusted. In order to estimate the linear and non-linear limb darkening coefficients, we interpolate the values computed for the TESS bandpass in Claret (2017). As an example, our best-fitting light curve model, phase-folded TESS observation data, and residuals of ID 116 are shown in Figure 4. To obtain formal uncertainties for the light curve model parameters, Monte Carlo simulations are applied using the JKTEBOP TASK8 feature. The best-fit solutions for TESS light curves of IDs 29, 67 and 116 using `jktebop` code and determined the $1\text{-}\sigma$ uncertainties using Monte Carlo and residual-permutation simulations are represented in Table 2. For the light curve models of ID 29 and 116, we assume circular orbit. However, $\text{ecc} * \cos(\text{omega}) = -0.0041462148 \pm 0.0000078612$, $\text{ecc} * \sin(\text{omega}) = -0.5891148379 \pm 0.0017385892$ and orbital eccentricity ($e = 0.5891294283$), periastron longitude omega ($w = 269.5967565681$ deg) for ID 67.

In addition to the photometric changes observed in the member binary stars resulting from eclipsing, we also noted additional intrinsic or extrinsic brightness variations in the residuals of the fits for these stars. These variations are not included in the light curve models and are treated separately (see in below).

2.2.2. Other variable stars

We perform periodogram analysis of the variations for the other discovered variable stars in UPK 220. We classify their variability type based on amplitude, period and behavior brightness changes in their light curves. A detailed analysis of each star and the results are presented in Section 4.2.

2.3. Stellar Atmospheric Parameters and SED Analysis of the Variable Members

Stellar atmospheric parameters are derived from photometry for eight member variable stars. For seven of these stars (IDs 29, 42, 49, 67, 116, 138 and 147), the surface gravity ($\log g$), metallicity ($[Fe/H]$) and the effective temperature (T_{eff}) are extracted using General Stellar Parameterize from Photometry (GSP-Phot) and Spectroscopy (GSP-Spec) methods which include four different algorithms (Andrae et al. 2023). These methods fit the low-resolution G_{BP}/G_{RP} spectra, G and parallax values of the stars.

For spectral energy distribution (SED) fitting, we use the open-source python package ARIADNE (Vines & Jenkins 2022). The package contains six different stellar atmosphere model grids and multiwavelength photometry to estimate T_{eff} , $[Fe/H]$ and $\log g$ of the stars. The SED fitting performed using *Bayesian Model Averaging* to obtain the best-fitted model parameters. To fit each SED of the variable member stars, we collected *2MASS* (J, H and K_s), *GaiaDR3* (G, G_{BP} , and G_{RP}), *Johnson* (U, B, V, R, and I), *PS1* (g, i, r, y, and z), *SDSS* (u, g, r, and i), *TESS* (Tmag), and *WISE* (W1, W2, W3 and W4) photometric data. It was not possible to obtain all the photometric data for each star. The data used in the SED fitting are listed in Appendix Table 8.

The atmospheric parameters of the stars derived from Gaia data and SED fitting are listed in Table 3 for binaries and Table 4 for single stars.

3. DETERMINATION OF FUNDAMENTAL CLUSTER PARAMETERS

To estimate the fundamental parameters of UPK 220, we focus on the member variable stars. We construct models of the stars using the Modules for Experiments in Stellar Astrophysics (MESA - Paxton et al. (2011, 2015, 2018, 2019)) stellar evolution code. Subsequently, the parameters derived from the variable stars have been used as model input parameters when constructing cluster isochrones in *MESA Isochrones and Stellar Tracks* (Dotter 2016; Choi et al. 2016, MIST). In constructing stellar interior models with MESA, we employ standard mixing length theory (Böhm-Vitense 1958) for convection treatment and utilise the Herwig approximation (Herwig 2000) for convective overshooting. OPAL opacity tables are taken from Iglesias & Rogers (1993, 1996)

and nuclear reaction rates are used from [Angulo et al. \(1999\)](#) with updated by [Kunz et al. \(2002\)](#) and [Cyburt et al. \(2010\)](#) in the models. We employ elemental diffusion from the *MESA* default option for stellar models that have a mass below $1.2 M_{\odot}$. We construct interior models using *MESASstar* and *MESABinary* packages to evolve single and binary stars, respectively.

3.1. Metallicity Determination

The stars within a specific cluster originate from a vast molecular cloud. Assuming the initial substances within the cloud are thoroughly blended, we can infer that all members of the cluster possess identical metallicity. This knowledge is essential for studying the local and global properties of galaxies. However, dealing with metallicity is not straightforward. While isochrone fitting in the color-magnitude diagram (CMD) can provide fairly precise results ([Dias et al. 2021](#)), it is not very sensitive to variations in metallicity.

In recent years, both individual studies and large-scale spectroscopic surveys, such as the one discussed by [Netopil et al. \(2022\)](#), have significantly advanced our understanding of the Galactic metallicity distribution based on OCs. Despite the increased availability of physical parameters for numerous clusters from the Gaia database, metallicity remains a source of uncertainty. Even known metallicity values for clusters often stem from spectral data of only one or a few stars.

In light of this, our study aims to enhance parameter estimation by leveraging distinctive features of specific stars within the cluster, utilizing TESS data from member stars.

We employed an automated tool called *Metalcode*³ for the determination of parameters of clusters, such as reddening, age, and metallicity, applying iterative processes derived from methods developed by [Poehnl & Paunzen \(2010\)](#). In *Metalcode*, astrophysical parameters of UPK 220 are derived from isochrone grids by eliminating distance and reddening as free parameters. This allows the tool to focus on deriving the metallicity of the cluster with high precision. The initial estimations are iteratively refined by comparing observed data in the normalised temperature-luminosity diagram that is driven by the isochrone grids. Also, *Metalcode* is capable of computing the three fundamental parameters of the cluster: $E(G_{BP} - G_{RP})$, t , and $[Fe/H]$, performed for Johnson B and V , 2MASS J and K_s , and Gaia G , G_{BP} , and G_{RP} photometric systems ([Paunzen et al. 2023](#)). The process involves an automated χ^2 min-

imization technique that matches magnitudes and colors of the members with theoretical isochrones. The code works for the different metal abundance (Z) and age ($\log(t)$) values, starting from $Z = 0.001$ up to $Z = 0.040$, with a step as $\Delta Z = 0.001$, from $\log(t) = 6.6$ up to $\log(t) = 10.0$, with a step as $\Delta \log(t) = 0.01$, respectively. The isochrone fitting process iterates through various models of age, metallicity and extinction to find the best fit, ensuring accurate estimates of the cluster metallicity.

We have controlled the accuracy of the metallicity found from variable stars with this code. We assumed that the metallicity of the cluster members is the same. According to *Metalcode*, we found the best fit for the cluster fundamental parameters as follows: $d = 832$ pc corresponding to distance modulus $DM_0 = 9.6$ mag, $E(G_{BP} - G_{RP}) = 1.10$ mag corresponding to $E(B - V) = 0.85$ mag, $t = 200$ Myr, and $Z = 0.005$.

Metallicity values for 110 member stars were provided by GaiaDR3, with a median value of $[Fe/H] = -0.57$. This value is very close to the metallicity obtained using *Metalcode* ($[Fe/H] = -0.54$). Furthermore, we constrained the cluster metallicity through the variable stars, determined by three different methods, as seen in Table 4. However, for the reasons outlined below, our attention was directed towards the metallicity of three pulsating stars situated in close proximity to the blue part of the main sequence (MS), accurately representing the single stars within UPK 220. As seen in Table 4, although ID 16 has been identified as an evolved star ($\log g \simeq 3.95$), its brightness variations do not align with the evolved region of the isochrone. This issue, as discussed later in Section 4, raises some concerns about the membership of the star in the cluster. On the other hand, the metallicity values of ID 42 obtained from three methods are different from each other (see in Table 4). Due to these uncertainties, IDs 16 and 42 were excluded from consideration when determining metallicity. Since the metallicities obtained from GSP-Phot analysis are reliable and consistent with the error limits, the metallicity of three stars (IDs 49, 138 and 147) were considered in determining the input metallicity of MIST isochrones applied to the cluster. Thus, the average metallicity derived from these three variable single stars was calculated as $[Fe/H] = -0.56$, with $Z = 0.004$.

3.2. Determination of Physical Parameters

Despite metallicity being one of the four free parameters typically considered when fitting isochrones to the cluster MS, it is often ignored or assumed to be solar abundance in many studies. Consequently, an unknown bias is introduced in the estimation of the age, reddening

³ <https://github.com/mpiecka/metalcode>

ing, and distance of the cluster (Paunzen et al. 2010). Therefore, to demonstrate the effect of two different metallicities on the cluster parameters in the CMD of UPK 220, the results were examined in terms of solar abundance and the metallicity found by variable stars, as shown in Figure 5. Here, the red solid lines in the figure represent *MIST* isochrones with $[Fe/H] = -0.56$ (left panel) and solar abundance (right panel). Gray points on the diagram represent potential member stars, while stars marked in magenta and green circles represent the member variable stars classified as eclipsing binaries and the others, with their IDs listed in Table 1.

Our fitting procedure to determine cluster parameters from the CMD was as follows: Initially, we applied a CMD fit to all members assuming the solar metallicity (see in Figure 5, right panel), without including the metallicity constraints as given in Section 3.1. However, by considering the metallicity obtained from the variable stars and `Metalcode`, the *MIST* isochrone fit was reapplied to best represent the CMD of all member stars. After the constraining the metallicity, we obtained the age and distance of the cluster as shown in Figure 5 (left panel). We then compared the cluster parameters obtained from the variable stars and found them to be consistent with each other. These consistencies are discussed in the following section.

Based on the initial metallicities for the isochrones, the age and reddenings of the cluster were estimated as 140 Myr and $E(G_{BP} - G_{RP}) = 1.3$ mag for $[Fe/H] = -0.56$, and 110 Myr and $E(G_{BP} - G_{RP}) = 1.3$ mag for $[Fe/H] = [Fe/H]_{\odot}$, respectively. These reddenings correspond to $E(B - V) = 1.0$ mag for both metallicities, determined using the reddening ratio from Bragaglia et al. (2018). The isochrones were constructed with the intention of passing through the same turn-off point at both metallicities, and were fitted to provide the optimal fit.

While the differences in metallicity do not cause a significant difference in age and reddening, they do affect the distance modulus, with $DM_0 = 9.6$ mag for $[Fe/H] = -0.56$ and $DM_0 = 10.0$ for $[Fe/H] = [Fe/H]_{\odot}$. This difference leads to a distance discrepancy of nearly 200 pc and affects parameters such as mass (M), $\log g$, and T_{eff} obtained from the isochrone fit for the member variable stars. The parameters for the variable stars obtained for $[Fe/H] = -0.56$ can be seen in Table 4.

Since the effect of stellar rotation on the MS and, consequently, on the age is not observed in young clusters (40 to 300 Myr) (Yang et al. 2013; Akkaya Oralhan 2021), this effect has been neglected for one of the young

cluster UPK 220, and rotation has been disregarded in the isochrones.

4. ANALYSIS RESULTS OF MEMBER VARIABLE STARS

The brightness changes of member variable stars obtained from the TESS analysis are represented in Figure 5 as error bars in both the G and $(G_{BP} - G_{RP})$ planes. The binary sequence (BS) for equal mass systems ($q = 1$) is shown as a blue solid line in the left panel. Accordingly, except for a few stars (IDs 16 and 29), the majority of the member variable stars approach the MS within these brightness limits or fall between the MS and the BS. The stars with IDs 16 and 29, which could potentially be cluster members, do not coincide with the cluster MS and BS. Although ID 16 shows a deviation from the cluster MS, the position of ID 29 coincides with the MS and BS within the brightness change limits. This raises questions about the accuracy of the age determined for the cluster or whether this star is a member of the cluster. If these stars (IDs 16 and 29) are indeed potential members of the cluster, the cluster age should shift towards older ages. However, the presence of the stars that are well fitted with the 140 Myr isochrone above the member variable stars and one evolved star located in the subdwarf region points to younger ages.

4.1. Binaries

The dynamical evolution of a star cluster is heavily influenced by its binary population. Even a small initial fraction of binary stars can have a considerable impact on cluster dynamics and the overall evolution of the stellar population of the cluster. Since binary interactions (soft and hard) regulate internal energy and drive mass segregation, their existence influences the dynamical stability and lifetimes of OCs. The number of binary fractions, types of eclipsing binaries (detached, semi-detached and contact), and evolution of binary stars may have significant impacts on the dynamical evolution of OCs (Goodwin 2010; De Grijs et al. 2015; Piatti et al. 2017; Wang et al. 2022b).

Although an open star cluster contains a large number of binary systems, detecting all of them is quite challenging. According to Chen et al. (2024), approximately 50% of the member stars in clusters are expected to be binaries. It is evident that photometric data of Gaia is highly precise, Liu et al. (2025) found that binaries with $q < 0.5$ are difficult to detect using optical data alone. Similarly, despite Torres et al. (2021) having spectroscopic data spanning 39 years, the detection of lower-mass binaries remains constrained due to uncertainties in orbital periods and orbital inclinations.

In addition, due to the availability of photometric TESS data, only eclipsing binaries with short periods (up to ~ 27 days) can be discovered. Furthermore, due to the infrared sensitivity of TESS data, it is highly likely that many of these binaries remain undetected. In this study, considering the number of member stars in UPK 220, at least 70 stars are expected to be binaries. However, due to the fact that mentioned above regarding TESS, only three binary stars have been detected.

It is commonly understood that an unresolved binary system, consisting of two identical stars, exhibits the same color but twice the luminosity compared to a single star with equivalent properties. Additionally, such a system, composed of two MS stars with $q = 1$, will manifest a vertical displacement of 0.753 mag in the cluster CMD, regardless of the wavelength bands utilized (Hurley & Tout 1998). A system with two unequal MS components will exhibit a combined color that is redder than that of the brighter component. Its luminosity is higher than that of a single star but lower than that total luminosity of an equal-mass binary (Hurley & Tout 1998). The difference in colors and magnitudes is influenced by the mass ratio $q = M_1/M_2 \leq 1$ where M_1 and M_2 represent the masses of the primary and secondary components, respectively. As q approaches zero, the position of the binary will converge towards the MS, since the impact of the fainter component becomes negligible (Yalyalieva et al. 2024).

As mentioned above, the positions of the binary stars in the CMD (as shown with green circles in Figure 5) may vary depending on the mass ratios of the system and their respective contributions to the total radiation. Since the parameters are determined based on the total brightness of the binary, the results may be misleading depending on the contributions from each component. Additionally, the *Gaia* brightness given in the CMD may vary depending on the phase of the binary system at the time of observation. Since the *Gaia* database provides average brightnesses for any star, it is inevitable that brightness differences will be observed for the variable stars between observations. Therefore, instead of *Gaia* magnitudes, the T_A and T_B magnitudes of each component obtained from *TESS* light curves were used in this study. Converting *TESS* to *Gaia* bandpasses, we use the relation in Stassun et al. (2019).

When we check the positions of these stars on the CMD, IDs 29 and 67 have abnormal positions and are displaced from the MS. Considering the phases of these stars and their positions to the MS, comparisons of these stars with the model results are as follows:

- **ID 29:** The system is a detached binary and in addition to primary and secondary eclipses, ellip-

soidal effect is also clearly seen as a sinusoidal variation in the light curve of the star (see in Figure 6). In the light curve of the star, six primary minima (from 2458764.5 to 2458765.0 BJD in sector 17, from 2458802.0 to 2458803.5 BJD in sector 18, from 2458955.0 to 2458956.0 BJD and from 2458968.0 to 2458969.5 BJD in sector 24, from 2459853.0 to 2459853.5 BJD in sector 57) and three secondary (from 2458968.0 to 2458969.5 BJD in sector 24, from 2459903.4 to 2459903.6 BJD and from 2459910.0 to 2459910.1 BJD in sector 58) appear distorted.

On the other hand, there is no data for the out-of-eclipse portion of the *TESS* light curve of ID 29 during the following intervals: from 2458791.0 to 2458791.5 BJD in sector 17, from 2459860.5 to 2459861.0 BJD in sector 57 and from 2459882.0 to 2459882.5 BJD, from 2459889.0 to 2459890.0 BJD and from 2459896.0 to 2459896.5 BJD in sector 58.

For the light curve models of ID 29, we assume circular orbit because the system has orbital periods lower than 5 days (Geller et al. 2013). According to the mass values of M_A and M_B obtained from *MESA* binary models, the mass ratio was calculated to be $q = 0.6$.

When the GSP-Phot and SED values based on the total brightness are compared to the *MESA* binary model, there are differences in temperature. While GSP-Phot and SED temperatures are consistent with each other (~ 9500 K), the *MESA* model yields $T_{\text{eff,A}} = 11500$ K and $T_{\text{eff,B}} = 8900$ K for M_A and M_B , respectively. However, when considering the contributions of both components to the system temperature, these values fall within the effective temperature ranges derived by GSP-Phot and SED, indicating that reasonable results are obtained from *MESA* binary model.

- **ID 67:** The light curve of ID 67 represents a typical detached eclipsing binary system containing a pulsating component. In *TESS* observation of the star, data gaps of totally ~ 1.5 , ~ 1.4 , ~ 1 , ~ 4 and ~ 1 days were encountered in sectors 17, 18, 24, 57 and 58, respectively. Nevertheless, it has been noticed that none of these data gaps impact primary and secondary minima in our analysis.

A total of five primary minima and six secondary minima were analyzed in this study. We have clearly seen the variations in the residuals of the fits (see in Figure 6). We therefore perform a Lomb-Scargle analysis for the star and discover Cepheid-like pulsations with a period of ~ 2.5 days.

The derived pulsating frequencies with their amplitudes, phases and estimated periods of each sector TESS observations are presented with their uncertainties in Table 5.

We consider the light curve brightness change behaviour and period of the system that the companion is a classical Cepheid (δ Cephei-type). Classical Cepheids are intermediate-mass, young stars (Plachy et al. 2021). In this respect, our MESA model results for ID 67 are consistent in terms of age and mass. However, spectral observations are essential to achieve more precise results.

The presence of a Cepheid component in ID 67 allowed for a comparison of the GaiaDR3 distance. We calculated the distance of the star as 987 ± 37 pc using Gaia parallax and 1148 ± 205 pc using the period-luminosity relation in Owens et al. (2022). This discrepancy in distance may arise from factors such as metallicity, parallax offset, orbital parallax, or the effects of binary evolution on Cepheid variables. For example, when orbital parallax is included, according to the calculations of Groenewegen (2023), there is approximately a 5% change in the GaiaDR3 parallax. Under this assumption, the distance of ID 67 is calculated to be between 924 and 1060 pc.

As shown in Table 3, T_{eff} and $logg$ values obtained from GSP-Phot and SED analyses for the components A and B are consistent, indicating a similar evolutionary stage. However, the MESA model results reveal that the higher-mass component is hotter than the lower-mass component. For the metallicity, the most of the effective temperature contribution in the SED and GSP-Phot analysis comes from the high-mass component.

Examining the CMD position of the system, the Gaia brightness places it in the BS. However, due to the large brightness variations, estimating mass ratios directly from the BS is challenging. Based on the TESS brightness variations and the mass values derived from models, there is an approximate twofold difference in mass between the components, explaining the significant brightness variation.

Additionally, the presence of pulsation in the system causes the brightness variation to be very large, as seen in Figure 6. Furthermore, the very similar results found in the two MESA models reduce the margin of error in mass values, and this is supported by other parameters. Considering the mass ratio of $q = 0.5$, this indicates that the B

component is more evolved. Indeed, the $logg$ value supports that the B component is more evolved.

- **ID 116** : The system is a detached eclipsing binary. The TESS light curve of the star, derived from sectors 17, 18, 24, 57 and 58, contains a total of 18 primary and 14 secondary minima but unfortunately, three secondary minima have incomplete or data gaps. Additionally, the out-of-eclipse data of ID 116 observed in five different sectors in total exhibits an intermittent data gap of ~ 11 days.

We conducted Lomb-Scargle analysis of the residuals for the star and found low-amplitude pulsation with a period of ~ 5.5 days, observed only in the TESS data for sectors 57 and 58. The derived pulsation frequencies, along with their amplitudes, phases and estimated periods from the residuals are presented with their uncertainties in Table 5. We assumed *BTSettle* fit for primary star and a blackbody fit for component stars of ID 116. Through SED analysis, the two components of the system were photometrically distinguished, and the T_{eff} and $logg$ values were determined, separately. However, since T_{eff} obtained from GSP-Phot is derived from the total brightness of the binary system, it is not compatible with those obtained from SED. Although the T_{eff} values obtained from the MESA model are compatible with each component, separately. There is an incompatibility between the $logg$ values obtained from SED analysis and MESA models. According to the mass values obtained from the MESA models, $q \simeq 0.67$, and the brightness obtained from GaiaDR3 is also within this range.

4.2. Other Variables

- **ID 16**: Using TESS data, we estimated the rotation period of the star as $P_{rot} = 3.061 \pm 0.025$ days. Light curve of ID 16 exhibits spot modulations, similar to observed in magnetic active stars. (e.g. HD 176330 - Bowman et al. (2018), TIC 219234021 - Sikora et al. (2019)). Additionally, we find another period equal to $P_{rot}/2$. We doubt that the spots on the star are separated by 180° in longitude (aka AU Mic-like effect - Martin et al. (2024)).

Using gyrochronology relation from Barnes (2007), we determined the stellar age to be 136 ± 21 Myr using P_{rot} of the star. The star is located at a point very far from the MS in the CMD and does not approach the MS, even when the brightness change is taken into account. Despite this, all parameters

found in the SED and GSP-Spec analyses were compatible with each other.

- **ID 42:** The light curve of ID 42 was derived using TESS observations from sectors 17, 18, 24, 57 and 58. Similar to ID 16, the star displays spot modulations that are evident in the TESS light curve. We estimate the rotation period of the star as 1.691 ± 0.008 days by using Lomb-Scargle period analysis.

However, the gyrochronology relation of Barnes (2007) is unable to accurately determine the stellar ages with $P_{\text{rot}} \leq 2$ days. Therefore, we estimate the minimum age of the star to be 50 Myr. In the CMD, the star is located close to the MS, and its brightness variation as a variable star is relatively small. The mass value obtained from the MESA model is approximately $M = 1.40 M_{\odot}$. The T_{effS} derived from the GSP-Phot (~ 8000 K) and SED (~ 7500 K) analyses are very close to each other, although they are slightly lower than obtained from the MESA model (~ 8500 K).

- **ID 49:** The star exhibits a classical γ Dor behavior in the TESS light curve. We identified gravity (g-) mode pulsation of ID 49 through Lomb-Scargle periodogram analysis. The fundamental period was determined to be 0.6663 ± 0.0028 days. The pulsation frequencies of the star are listed in Table 6. Although g-mode pulsations can be used to estimate the age of γ Dor stars (Mombarg et al. 2019), the TESS data of ID 49 are insufficient to obtain g-mode period spacings. This issue can be addressed in the future with long-term continuous observations.

γ Dor stars, one of the well-known non-radial pulsating variables, fall within the spectral-type range between late-A and early F-type stars. They exhibit a characteristic light curve variations and their period range varies between ~ 0.3 and ~ 3.5 days (Handler 1999). The light curve variation and fundamental pulsation period range indicates that ID 49 is a γ Dor variable candidate. Considering the classical instability strip, γ Dor stars are typically found within the range of 7000-10000 K (Dupret et al. 2005). The T_{eff} of ID 49, determined as 8577_{-82}^{+74} from GSP-Phot and 8353_{-89}^{+71} from SED analysis, supports its classification as a γ Dor variable.

Previous studies have not identified γ Dor variables in OCs older than ~ 250 Myr (Krisciunas & Patten 1999). Therefore, it provides further

evidence that the age of the UPK 220 cluster is less than ~ 250 Myr, consistent with findings in this study. Nevertheless, there are also studies in the literature that present evidence to the contrary. Among these, a comprehensive study that also takes $[Fe/H]$ of clusters into consideration was conducted by Molenda-Żakowicz et al. (2009). They found that the relation between cluster age and $[Fe/H]$ of an OC and the probability of observing a γ Dor variable in an OC is not dependent on the cluster age. Furthermore, they result that the probability of observing a γ Dor increases with $[Fe/H]$ in the cluster after a certain age as $\log(\text{age}) \simeq 8.5$. However, they also emphasise that the membership of γ Dor stars discovered in these OCs should be carefully reconsidered.

Upon examination of the studies about γ Dor stars in OCs (Piatti et al. 1995; Gratton 2000; Schuler et al. 2003; Burke et al. 2003; Carretta et al. 2004; Pace et al. 2008; Santos et al. 2009; Joshi et al. 2012), it was determined that UPK 220 is one of the two clusters (the other is NGC 581 - Tadross (2003)) with a metal-poor γ Dor member among the Galactic OCs exhibiting such variables.

As shown in Table 3, all T_{eff} values obtained from the GSP-Phot and SED analysis, and MESA models are compatible with each other. The mass value was found to be $M = 1.40 M_{\odot}$. This mass is consistent with the range of γ Dor mass ($1.4 - 2.0 M_{\odot}$ - Takata et al. (2020)).

- **ID 138:** The light curve exhibits a periodic variation with a period of 1.15926 ± 0.00166 days and the amplitude of the variation is roughly 1%. The position of the star on CMD, the period between 0.01 and 5 days, and the amplitude of the variation (Percy et al. 2006) indicate that the star is a T-Tauri candidate. However, the lack of observational data in the infrared region of the spectrum precludes a definitive conclusion regarding the red excess of the star, as determined on SED.

Herbst et al. (1994) divides T-Tauri stars into three subtypes based on their photometric variations. ID 138 appears to belong to the Type I class as it exhibits cyclic variations with low amplitude modulation. Herbst et al. (1994) also note that the stars of Type I class display rotational modulation due to cool spots and have no visible accretion disks in their spectroscopy. However, due to the lack of spectroscopic observations of ID 138, it is not possible to reach a definitive conclusion on this issue.

The star is located in the faint part of the MS in the CMD, and its mass, derived from the MESA model, is estimated to be $M = 0.70 M_{\odot}$. The T_{eff} s from the GSP-Phot and SED analyses are lower than those predicted by the MESA model, with the T_{eff} range of the star varying between 4400 and 5300 K. The relatively low mass and cooler temperature compared to the Sun further support the classification of ID 138 as a T-Tauri star candidate.

- **ID 147:** Upon analysis of the TESS light curve of the star, similar to ID 138, it may be a potential Type I class T-Tauri star candidate within UPK 220. This conclusion is based on the estimated period and amplitude of the variation (~ 2 mmag). The light curve of ID 147 exhibits spot modulations with a period of 2.857 ± 0.004 days. Utilising the rotation period of the star in the gyrochronology relation from Barnes (2007), we estimate the stellar age to be 194 ± 56 Myr.

Due to the lack of observational data in the infrared region, it is not possible to confirm the presence of an accretion disk based on the SED of the star. It is evident that further spectral observations are necessary to substantiate the presence of the disk around the star. The star is low-mass, and its position in the CMD, located in the fainter region of the MS, is compatible with its mass $M = 0.80 M_{\odot}$ that is derived from MESA model. The parameters derived from GSP-Phot and SED analysis, and MESA also yielded comparable results (see in Table 4).

5. DISCUSSION

We assume that stars with membership probabilities $P \geq 0.725$ are the most probable members of UPK 220. Using the probability range, we derived mean proper motions as $\mu_{\alpha} \cos(\delta) = -2.41 \pm 0.11$ mas/yr and $\mu_{\delta} = -2.64 \pm 0.12$ mas/yr. This proper motions are consistent with those reported by Hunt & Reffert (2024) as ($\mu_{\alpha} = -2.41$ and $\mu_{\delta} = -2.47$ mas/yr).

The structural parameters of UPK 220 derived from the King profile fitting are as follows: the central stellar density $\sigma_{\text{ok}} = 0.835 \pm 0.121$ stars/arcmin², the core radius $R_c = 5.751 \pm 1.079$ arcmin, the residual stellar background density $\sigma_{\text{bg}} = 0.674 \pm 0.023$ stars/arcmin², and the limit radius $R_{\text{lim}} = 24.0$ arcmin. The radius is compatible with the findings of Hunt & Reffert (2024) as $r_{50} = 0.213^{\circ}$ (corresponds to a physical size of 7.02 pc). They define the cluster radius as 50 % of member stars within the tidal radius. Besides, $R_c = 6.15$ arcmin

and $R_{\text{lim}} = 23.57$ arcmin that are given in Sim et al. (2019) are quite consistent with our results.

We conclude that the number of member stars (N_m) within the limiting radius of UPK 220 is 148. This value shows considerable discrepancies compared to studies in the literature: Sim et al. (2019) ($N_m = 102$), Castro-Ginard et al. (2020) ($N_m = 91$), Tarricq et al. (2022) ($N_m = 664$, $0.1 \leq P \leq 1.0$), Hunt & Reffert (2024) ($N_m = 323$, $0.45 \leq P \leq 1.0$), and Alfonso et al. (2024) ($N_m = 286$). These discrepancies in N_m arise due to differences in the adopted probability range and the lower limit of photometric selection criteria within the cluster field.

Our results align with the membership estimation by Cantat-Gaudin et al. (2020), except that variable star ID 138, identified in our study, is not listed as a member in their catalog. It is important to point out that in Table 7, we compare the results of Cavallo et al. (2023) that is based only on their 84th percentile predictions.

In Table 7, the astrophysical parameters of UPK 220 are compared with those reported in the literature. Since the studies (Sim et al. 2019; Cantat-Gaudin et al. 2020; Tarricq et al. 2022; Cavallo et al. 2023) do not directly report [Fe/H] metallicities, we converted the provided metal abundance Z to [Fe/H] using an analytical expression from Bovy⁴. As shown in Table 7, our estimated DM and d , which are crucial for determining the fundamental parameters of the cluster, align well with the values reported in the literature. However, notable discrepancies exist in our age, metallicity, and reddening with respect to the literature. The aforementioned discrepancies between our results and the literature can be attributed to four factors: the type of photometric data used (GaiaDR2, GaiaEDR3, or GaiaDR3), the lower limit of the adopted photometric range, the membership selection criteria (probability thresholds), and the metallicity considered. We infer that these discrepancies primarily result from differences between our adopted metallicity, as well as the types of isochrones employed in the analyses. To ensure the consistency of physical parameter space between the cluster and the member variable stars within the cluster region, we utilized MIST isochrones, derived from MESA models. Due to the fact that the MESA models are also considered for the member variable stars. In contrast, all age estimations reported in the literature are obtained from PARSEC isochrones (Bressan et al. 2012) with different metallicities, considering the solar metal abundance. It

⁴ <https://github.com/jobovy/isodist/blob/master/isodist/Isochrone.py>

should be noted that this study presents the first direct determination of [Fe/H] for UPK 220, combining results from `Metalcode`, MESA models, SED analyses of the member variable star and GSP-Phot and GSP-Spec.

6. CONCLUSIONS

In this study, the fundamental parameters of UPK 220 were determined by analysing the variable stars within the cluster, while simultaneously constraining the parameters of the variable stars using these cluster parameters. To achieve this, we combined GaiaDR3 and TESS photometric observations. Using GaiaDR3, we derive fundamental parameters of UPK 220 through membership analyses, and with TESS, we discover the member variable stars belonging to the cluster.

Although we have presented a different approach to cluster analysis using the most recent astrometric and photometric data in our study. Our research demonstrates the need for follow-up ground-based spectral and

photometric observations to determine fundamental parameters more accurately for the variable member stars of UPK 220.

Acknowledgements: This study was supported by Scientific and Technological Research Council of Turkey (TUBITAK) under the Grant Number 122F364. The authors thank to TUBITAK for their supports.

Facilities: Gaia(DPAC), TESS(SPOC)

Software: astropy (Astropy Collaboration et al. 2018), matplotlib (Hunter 2007), numpy (Harris et al. 2020), astroquery (Ginsburg et al. 2019), Lightkurve (Lightkurve Collaboration et al. 2018), MESA (Paxton et al. 2011, 2015, 2018, 2019), TESScut (Brasseur et al. 2019), ARIADNE (Vines & Jenkins 2022), JKTEBOP (Southworth et al. 2004)

REFERENCES

- Ahumada, A. V., Cignoni, M., Bragaglia, A., et al. 2013, Monthly Notices of the Royal Astronomical Society, 430, 221
- Akkaya Oralhan, İ. 2021, Journal of Astrophysics and Astronomy, 42, 60, doi: [10.1007/s12036-021-09757-9](https://doi.org/10.1007/s12036-021-09757-9)
- Alfonso, J., García-Varela, A., & Vieira, K. 2024, A&A, 689, A18, doi: [10.1051/0004-6361/202450901](https://doi.org/10.1051/0004-6361/202450901)
- Almeida, A., Monteiro, H., & Dias, W. S. 2023, Monthly Notices of the Royal Astronomical Society, 525, 2315
- Andrae, R., Fouesneau, M., Sordo, R., et al. 2023, A&A, 674, A27, doi: [10.1051/0004-6361/202243462](https://doi.org/10.1051/0004-6361/202243462)
- Angulo, C., Arnould, M., Rayet, M., et al. 1999, NuPhA, 656, 3, doi: [10.1016/S0375-9474\(99\)00030-5](https://doi.org/10.1016/S0375-9474(99)00030-5)
- Astropy Collaboration, Price-Whelan, A. M., Sipőcz, B. M., et al. 2018, AJ, 156, 123, doi: [10.3847/1538-3881/aabc4f](https://doi.org/10.3847/1538-3881/aabc4f)
- Barnes, S. A. 2007, ApJ, 669, 1167, doi: [10.1086/519295](https://doi.org/10.1086/519295)
- Bedding, T. R., Murphy, S. J., Crawford, C., et al. 2023, ApJL, 946, L10, doi: [10.3847/2041-8213/acc17a](https://doi.org/10.3847/2041-8213/acc17a)
- Böhm-Vitense, E. 1958, ZA, 46, 108
- Bonatto, C., & Bica, E. 2005, Astronomy & Astrophysics, 437, 483
- Bonatto, C., Santos, J., & Bica, E. 2006, Astronomy & Astrophysics, 445, 567
- Bowman, D. M., Buysschaert, B., Neiner, C., et al. 2018, A&A, 616, A77, doi: [10.1051/0004-6361/201833037](https://doi.org/10.1051/0004-6361/201833037)
- Bragaglia, A., Fu, X., Mucciarelli, A., Andreuzzi, G., & Donati, P. 2018, A&A, 619, A176, doi: [10.1051/0004-6361/201833888](https://doi.org/10.1051/0004-6361/201833888)
- Brasseur, C. E., Phillip, C., Fleming, S. W., Mullally, S. E., & White, R. L. 2019, Astrocut: Tools for creating cutouts of TESS images, Astrophysics Source Code Library, record ascl:1905.007. <http://ascl.net/1905.007>
- Breger, M., Stich, J., Garrido, R., et al. 1993, A&A, 271, 482
- Bressan, A., Marigo, P., Girardi, L., et al. 2012, Monthly Notices of the Royal Astronomical Society, 427, 127
- Burke, C. J., Depoy, D. L., Gaudi, B. S., & Marshall, J. L. 2003, in Astronomical Society of the Pacific Conference Series, Vol. 294, Scientific Frontiers in Research on Extrasolar Planets, ed. D. Deming & S. Seager, 379–382, doi: [10.48550/arXiv.astro-ph/0208305](https://doi.org/10.48550/arXiv.astro-ph/0208305)
- Cantat-Gaudin, T., Jordi, C., Vallenari, A., et al. 2018, Astronomy & Astrophysics, 618, A93
- Cantat-Gaudin, T., Anders, F., Castro-Ginard, A., et al. 2020, A&A, 640, A1, doi: [10.1051/0004-6361/202038192](https://doi.org/10.1051/0004-6361/202038192)
- Carretta, E., Bragaglia, A., Gratton, R. G., & Tosi, M. 2004, A&A, 422, 951, doi: [10.1051/0004-6361:20047142](https://doi.org/10.1051/0004-6361:20047142)
- Castro Ginard, A., Jordi i Nebot, C., Luri Carrascoso, X., et al. 2020, Astronomy & Astrophysics, 2020, vol. 635, num. A45
- Castro-Ginard, A., Jordi, C., Luri, X., et al. 2020, VizieR Online Data Catalog, J
- Cavallo, L., Spina, L., Carraro, G., et al. 2023, The Astronomical Journal, 167, 12
- Chehlaeh, N., Mkrtichian, D., Lampens, P., et al. 2018, Monthly Notices of the Royal Astronomical Society, 480, 1850

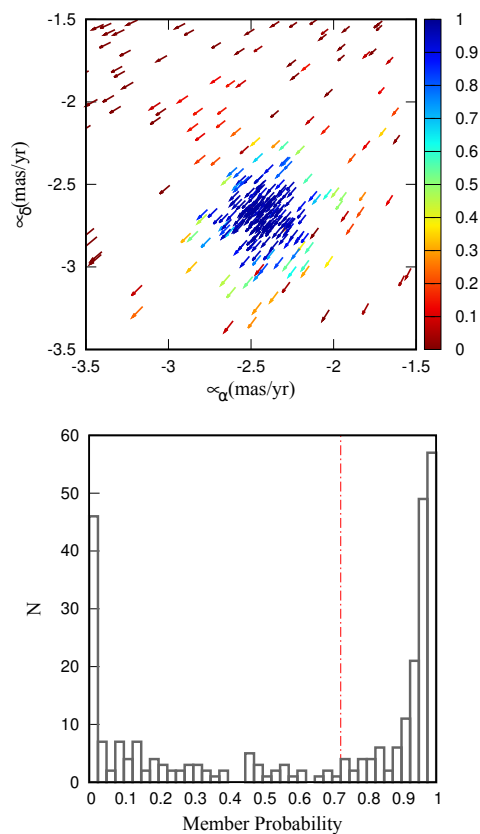


Figure 1. *Upper panel:* The proper motion vector diagram of UPK 220. The right colour bar represents the membership probabilities. *Lower panel:* The distributions of membership probabilities according to `pyUPMASK`. The vertical red dashed line shows the selected probability limit of 0.725.

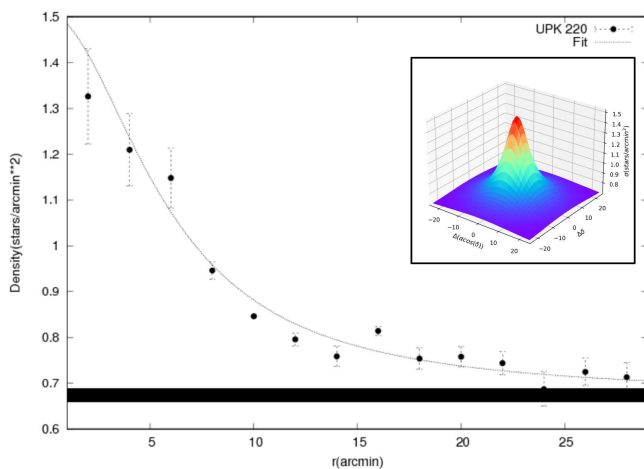


Figure 2. The radial density profile of UPK 220. The dotted curved line shows the fitting of King's profile. The horizontal black bar denotes the stellar background level measured in the comparison field. *Inserted plot on top:* The three-dimensional stellar surface density of UPK 220 accomplished by astrometric and photometric field star decontamination procedures on the cluster region.

Table 1. Properties of discovered member variable stars. The table contains member IDs, GaiaID, coordinates, proper motions with their errors, parallax, and member probability of these stars.

ID	GaiaID	RA (deg)	Dec (deg)	μ_α (mas/yr)	μ_δ (mas/yr)	ϖ (mas)	Prob.
16	2210486179667643008	350.94541734	66.57117234	-2.381 ± 0.010	-2.733 ± 0.011	1.041 ± 0.010	0.982
29	2210564038834839552	351.59436002	66.47981201	-2.505 ± 0.013	-2.679 ± 0.011	1.074 ± 0.010	0.980
42	2210470241050931456	351.54188195	66.48240523	-2.548 ± 0.027	-2.688 ± 0.024	1.034 ± 0.021	0.978
49	2210466908156116992	350.80052580	66.41964996	-2.465 ± 0.015	-2.556 ± 0.016	1.002 ± 0.013	0.977
67	2210490341492729216	350.80329554	66.62039368	-2.258 ± 0.021	-2.665 ± 0.021	1.013 ± 0.019	0.973
116	2210482541837015040	350.64660260	66.48970822	-2.619 ± 0.010	-2.712 ± 0.010	1.063 ± 0.009	0.944
138	2210487004303084544	351.30367105	66.59587931	-2.366 ± 0.111	-2.380 ± 0.099	1.057 ± 0.095	0.904
147	2210274390542367616	351.18580700	66.17499712	-2.296 ± 0.055	-2.623 ± 0.048	0.990 ± 0.047	0.847

Table 2. Best fit solutions for TESS light curves of IDs 29, 67 and 116 using `jktebop` code. Using Monte Carlo and residual-permutation simulations, we determined the $1\text{-}\sigma$ uncertainties. $ecc * \cos(\omega) = -0.0041462148 \pm 0.0000078612$, $ecc * \sin(\omega) = -0.5891148379 \pm 0.0017385892$ and orbital eccentricity ($e = 0.5891294283$), periastron longitude ω ($w = 269.5967565681$ deg) for ID67.

ID 29					
Parameter	Unit	Part 1 Sectors 17, 18	Part 2 Sector 24	Part 3 Sectors 57, 58	Adopted solution
Orbital Period (P_{orb})	[days]	1.69051 ± 0.00003	1.69049 ± 0.00007	1.69051 ± 0.00001	1.6905 ± 0.00008
Time of periastron (T_{p})	[days]	$2458766.44754 \pm 0.00046$	$2458957.47509 \pm 0.00054$	$2458855.20011 \pm 0.00362$	
Orbital inclination (i)	[deg]	70.902 ± 5.641	69.659 ± 4.319	81.393 ± 0.302	73.985 ± 7.111
Fractional radius of star A (r_{A})		$0.2597^{+0.0556}_{-0.0043}$	$0.2593^{+0.0015}_{-0.0013}$	$0.2711^{+0.0074}_{-0.0068}$	$0.2634^{+0.0049}_{-0.0049}$
Fractional radius of star B (r_{B})		$0.2252^{+0.0039}_{-0.0041}$	$0.2356^{+0.0015}_{-0.0016}$	$0.2562^{+0.0054}_{-0.0047}$	$0.2391^{+0.0044}_{-0.0048}$
Light ratio ($I_{\text{B}}/I_{\text{A}}$)		$0.5319^{+0.14503}_{-0.11617}$	$0.6102^{+0.06415}_{-0.05960}$	$0.6246^{+0.0394}_{-0.0358}$	$0.5889^{+0.1731}_{-0.1468}$
ID 67					
Orbital Period (P_{orb})	[days]	24.49314 ± 0.00031	24.41614 ± 0.00255	24.49260 ± 0.0005	24.49257 ± 0.0005
Time of periastron (T_{p})	[days]	$2458767.08336 \pm 0.00022$	$2458975.34104 \pm 0.00024$	$2459857.01723 \pm 0.00011$	
Orbital inclination (i)	[deg]	87.497 ± 0.026	88.302 ± 0.016	88.454 ± 0.017	88.398 ± 0.026
Orbital eccentricity (e)		$0.591^{+0.014}_{-0.007}$	$0.595^{+0.003}_{-0.005}$	$0.595^{+0.010}_{-0.005}$	$0.589^{+0.010}_{-0.005}$
Periastron longitude ω (w)	[deg]	$270.372^{+0.013}_{-0.007}$	$269.403^{+0.011}_{-0.029}$	$269.597^{+0.013}_{-0.005}$	$269.598^{+0.0106}_{-0.008}$
Fractional radius of star A (r_{A})		$0.0488^{+0.0011}_{-0.0023}$	$0.0380^{+0.0002}_{-0.0003}$	$0.0351^{+0.0049}_{-0.0049}$	$0.0367^{+0.0005}_{-0.0006}$
Fractional radius of star B (r_{B})		$0.0302^{+0.0003}_{-0.0005}$	$0.0275^{+0.0001}_{-0.0002}$	$0.0259^{+0.0044}_{-0.0048}$	$0.0272^{+0.0011}_{-0.0007}$
Light ratio ($I_{\text{B}}/I_{\text{A}}$)		$3.051^{+0.086}_{-0.156}$	$0.135^{+0.001}_{-0.001}$	$0.161^{+0.173}_{-0.147}$	$0.168^{+0.007}_{-0.004}$
ID 116					
Orbital Period (P_{orb})	[days]	7.56667 ± 0.00004	7.56675 ± 0.00009	7.56662 ± 0.00013	7.56668 ± 0.00016
Time of periastron (T_{p})	[days]	$2458765.83110 \pm 0.00015$	$2458962.56506 \pm 0.00013$	$2459893.26611 \pm 0.00015$	
Orbital inclination (i)	[deg]	86.380 ± 0.180	86.041 ± 0.220	85.794 ± 0.217	86.071 ± 0.358
Fractional radius of star A (r_{A})		$0.0743^{+0.0042}_{-0.0043}$	$0.0805^{+0.0015}_{-0.0013}$	$0.0822^{+0.0021}_{-0.00195}$	$0.0789^{+0.0049}_{-0.0049}$
Fractional radius of star B (r_{B})		$0.0684^{+0.0039}_{-0.0041}$	$0.0770^{+0.0015}_{-0.0016}$	$0.0763^{+0.0015}_{-0.0018}$	$0.0739^{+0.0044}_{-0.0048}$
Light ratio ($I_{\text{B}}/I_{\text{A}}$)		$0.6939^{+0.14503}_{-0.11617}$	$0.7506^{+0.06415}_{-0.05960}$	$0.69461^{+0.06950}_{-0.06711}$	$0.713^{+0.1731}_{-0.1468}$

Table 3. Spectral properties (effective temperature - T_{eff} , metallicity - $[Fe/H]$, surface gravity - $\log g$) and MESA model results (T_{eff} , $[Fe/H]$, $\log g$ and stellar mass - M) of member binary stars (system - A+B and components - A and B) with their IDs of UPK220 are presented. The spectral properties are derived by GSP-Phot and SED methods. Initial Helium and metallicity abundances are taken $Y_{\text{int}} = 0.2551$ and $Z_{\text{int}} = 0.0041$, respectively, for the MESA models of the binary member variable stars.

ID	T_{eff} (K)	$[Fe/H]$ (dex)	$\log g$ (dex)	M (M/M_{\odot})	System	Method
29	9565_{-95}^{+178}	$+0.31_{-0.12}^{+0.09}$	$3.76_{-0.02}^{+0.03}$	-	A+B	GSP-Phot
	9542_{-157}^{+196}	$-0.55_{-0.01}^{+0.01}$	$3.96_{-0.12}^{+0.11}$	-	A+B	SED
	11481	-0.56	4.26	3.2	A	MESA
	8912	-0.56	4.06	2.0	B	MESA
67	7330_{-71}^{+92}	$-1.08_{-0.05}^{+0.05}$	$3.95_{-0.01}^{+0.01}$	-	A+B	GSP-Phot
	7522_{-59}^{+86}	$-0.61_{-0.08}^{+0.06}$	$3.70_{-0.15}^{+0.17}$	-	A+B	SED
	11220	-0.56	4.27	3.1	A	MESA
	7244	-0.56	4.09	1.5	B	MESA
116	9216_{-30}^{+48}	$-0.76_{-0.02}^{+0.05}$	$3.78_{-0.01}^{+0.01}$	-	A+B	GSP-Phot
	4600_{-100}^{+100}	$-1.00_{-0.25}^{+0.25}$	$3.50_{-0.25}^{+0.25}$	-	A	SED
	5000_{-100}^{+100}	-	-	-	B	SED
	6025	-0.56	4.43	1.2	A	MESA
	4853	-0.56	4.63	0.8	B	MESA

Table 4. Same as in Table 3 but for single variable stars. For ID16, spectral properties are derived using GSP-Spec method.

ID	T_{eff} (K)	$[Fe/H]$ (dex)	$\log g$ (dex)	M (M/M_{\odot})	R (R/R_{\odot})	Method
16	7550_{-435}^{+250}	-	$3.95_{-0.15}^{+0.36}$	-	7.5	GSP-Spec
	7511_{-59}^{+68}	$-0.58_{-0.09}^{+0.07}$	$3.93_{-0.12}^{+0.14}$	-	-	SED
	7638	-0.56	4.41	1.3	1.2	MESA
42	7997_{-6}^{+2}	$-0.16_{-0.15}^{+0.09}$	$4.07_{-0.01}^{+0.02}$	-	1.9	GSP-Phot
	7470_{-111}^{+80}	$-0.37_{-0.11}^{+0.07}$	$4.03_{-0.12}^{+0.11}$	-	-	SED
	8390	-0.56	4.44	1.4	1.2	MESA
49	8577_{-82}^{+74}	$-0.47_{-0.06}^{+0.09}$	$4.20_{-0.07}^{+0.04}$	-	1.7	GSP-Phot
	8353_{-89}^{+71}	$-0.53_{-0.09}^{+0.06}$	$4.60_{-0.11}^{+0.12}$	-	-	SED
	8491	-0.56	4.45	1.5	1.2	MESA
138	4419_{-100}^{+81}	$-0.64_{-0.13}^{+0.21}$	$4.71_{-0.02}^{+0.02}$	-	0.7	GSP-Phot
	4939_{-90}^{+118}	$-0.58_{-0.14}^{+0.10}$	$4.69_{-0.14}^{+0.11}$	-	-	SED
	4508	-0.56	4.73	0.6	0.6	MESA
147	5412_{-41}^{+51}	$-0.57_{-0.09}^{+0.07}$	$4.59_{-0.02}^{+0.03}$	-	1.0	GSP-Phot
	5300_{-85}^{+108}	$-0.61_{-0.09}^{+0.06}$	$4.22_{-0.13}^{+0.15}$	-	-	SED
	5598	-0.56	4.64	0.8	0.7	MESA

Table 5. Lomb-Scargle periodogram analysis of *TESS* observations of ID67 and ID 116. Derived frequencies of pulsation (in c/d unit) with their amplitudes (in mag unit), phases (in rad/ 2π unit) and estimated periods (in days unit) from the residuals are presented with their uncertainties. S1718, S24, and S5758 refer to sectors 17 and 18, 24, and 57 and 58 of *TESS* observations, respectively.

ID	Frequency (c/d)	Amplitude (mag)	Phase (rad/ 2π)	Period (day)	Sectors
67	0.8496901 ± 0.0021476 (<i>f</i>)	$0.0024 \pm 4.66\text{e-}05$	0.0844 ± 0.0031	1.177 ± 0.006	S1718
	0.8434911 ± 0.0005211 (<i>f</i>)	$0.0013 \pm 3.18\text{e-}05$	0.3893 ± 0.0041	1.186 ± 0.002	S24
	0.8449160 ± 0.0001094 (<i>f</i>)	$0.0023 \pm 2.55\text{e-}05$	0.0256 ± 0.0018	1.184 ± 0.001	S5758
116	0.1842825 ± 0.0024367 (<i>f</i>)	$0.0002 \pm 1.88\text{e-}05$	0.0997 ± 0.0139	5.426 ± 0.139	S5758
	0.3415368 ± 0.0025788 (<i>f/2</i>)	$0.0002 \pm 1.88\text{e-}05$	0.8737 ± 0.0151	2.928 ± 0.044	S5758

Table 6. Lomb-Scargle periodogram analysis of *TESS* observations in all sectors of ID 49. Derived frequencies of pulsation (in c/d unit) with their amplitudes (in mag unit) and phases (in rad/ 2π unit) are presented.

ID	Frequency (c/d)	Amplitude (mag)	Phase (rad/ 2π)
f1	0.0202850	0.0022	0.2341
f2	1.5019749	0.0018	0.5717
f3	0.0511536	0.0021	0.4037
f4	0.0679108	0.0017	0.4499
f5	0.1331757	0.0021	0.5337
f6	1.3529241	0.0012	0.7303
f7	0.1173004	0.0018	0.9738
f8	0.1737458	0.0016	0.3178
f9	0.1922669	0.0011	0.2162
f10	0.0987793	0.0007	0.1113
f11	1.3767368	0.0006	0.4531
f12	0.2654694	0.0007	0.2894
f13	0.2196076	0.0008	0.8653
f14	0.1552246	0.0007	0.2997
f15	0.0837861	0.0008	0.1004
f16	0.2407746	0.0005	0.2581
f17	0.0335144	0.0008	0.3487
f18	1.5240239	0.0003	0.7271
f19	1.2250401	0.0003	0.3399
f20	1.6289769	0.0003	0.7256
f21	0.3280885	0.0003	0.9015

Table 7. Fundamental parameters comparison with the literature for UPK 220.

E(B-V)	$(V_0 - M_V)$	d (kpc)	[Fe/H]	log(Age)	Age (Myr)	Isochrome	Photometry	Ref.
1.3	9.60	0.967	-0.56	8.15	140.0	MIST	GaiaDR3, G, G _{BP} , G _{RP}	This paper
-	-	0.967 ± 0.28	0.127	8.75	562.34	PARSEC	GaiaDR2 Gaia G, G _{BP} , G _{RP}	Sim et al. (2019)
0.70	9.98	0.99	0.0	8.04	109.65	PARSEC	GaiaDR2, Gaia G, G _{BP} , G _{RP}	Cantat-Gaudin et al. (2020)
0.880 ± 0.071	-	0.950 ± 0.12	0.029 ± 0.129	7.295 ± 0.329	19.72	PARSEC	GaiaDR2, Gaia G, G _{BP} , G _{RP}	Dias et al. (2021)
-	-	0.964	0.0	8.08	120.23	PARSEC	Gaia EDR3, Gaia G, G _{BP} , G _{RP}	Tarricq et al. (2022)
0.90 ± 0.052	-	0.944 ± 0.009	0.025 ± 0.097	7.477 ± 0.290	29.99	PARSEC	Gaia EDR3, Gaia G, G _{BP} , G _{RP}	Almeida et al. (2023)
0.98	10.31	1.153	0.75	8.01	102.33	PARSEC	GaiaDR3, Gaia G, G _{BP} , G _{RP} ; 2MASS J,H	Cavallo et al. (2023)
0.70	9.98	0.997	0.301	7.72	52.48	PARSEC	GaiaDR3 G, G _{BP} , G _{RP}	Alfonso et al. (2024)

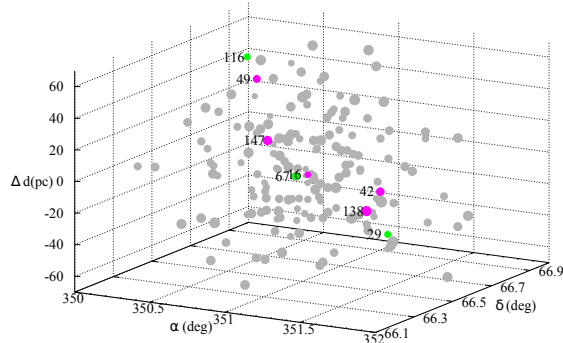


Figure 3. Three dimensional distribution of the cluster members with eight member variable stars. The dot size of the stars corresponds to G_{mag} .

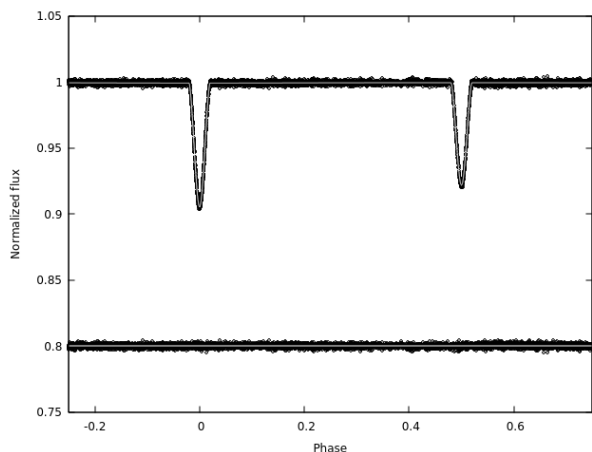


Figure 4. The best fit model (solid line) and residuals (at 0.8) that is obtained by `jktebop` and observed TESS light curve of ID 116 at sectors 57 and 58. From the observed primary minima, the ephemeris (E) and phases determined as $T_{\text{primin}} = (2459893.26611 \pm 0.00015) + (7.56662 \pm 0.00013)E$.

Chen, X., Liu, Z., & Han, Z. 2024, *Progress in Particle and Nuclear Physics*, 134, 104083,

doi: <https://doi.org/10.1016/j.pnpnp.2023.104083>

Chi, H., Wei, S., Wang, F., & Li, Z. 2023, *The Astrophysical Journal Supplement Series*, 265, 20

Choi, J., Dotter, A., Conroy, C., et al. 2016, *ApJ*, 823, 102, doi: [10.3847/0004-637X/823/2/102](https://doi.org/10.3847/0004-637X/823/2/102)

Claret, A. 2017, *A&A*, 600, A30, doi: [10.1051/0004-6361/201629705](https://doi.org/10.1051/0004-6361/201629705)

Cutri, R., Skrutskie, M., Van Dyk, S., et al. 2003, *VizieR online data catalog*, II

Cybur, R. H., Amthor, A. M., Ferguson, R., et al. 2010, *ApJS*, 189, 240, doi: [10.1088/0067-0049/189/1/240](https://doi.org/10.1088/0067-0049/189/1/240)

Dar, A. A., Parihar, P. S., Saleh, P., & Malik, M. A. 2018, *New Astronomy*, 64, 34

De Grijs, R., Li, C., & Geller, A. M. 2015, *Proceedings of the International Astronomical Union*, 12, 222

Dias, W., Alessi, B., Moitinho, A., & Lépine, J. 2002, *Astronomy & Astrophysics*, 389, 871

Dias, W. S., Monteiro, H., Moitinho, A., et al. 2021, *MNRAS*, 504, 356, doi: [10.1093/mnras/stab770](https://doi.org/10.1093/mnras/stab770)

Dotter, A. 2016, *ApJS*, 222, 8, doi: [10.3847/0067-0049/222/1/8](https://doi.org/10.3847/0067-0049/222/1/8)

Dupret, M. A., Grigahcène, A., Garrido, R., Gabriel, M., & Scuflaire, R. 2005, *A&A*, 435, 927, doi: [10.1051/0004-6361:20041817](https://doi.org/10.1051/0004-6361:20041817)

Durgapal, A., Rangwal, G., Bisht, D., et al. 2020, *Journal of Astrophysics and Astronomy*, 41, 1

Frasca, A., Alonso-Santiago, J., Catanzaro, G., et al. 2023, *A&A*, 677, A154, doi: [10.1051/0004-6361/202347226](https://doi.org/10.1051/0004-6361/202347226)

Friel, E. 1995, *Annual Review of Astronomy and Astrophysics*, 33, 381

Fritzewski, D. J., Van Reeth, T., Aerts, C., et al. 2024, *A&A*, 681, A13, doi: [10.1051/0004-6361/202347618](https://doi.org/10.1051/0004-6361/202347618)

Gaia Collaboration, Vallenari, A., Brown, A. G. A., et al. 2023, *A&A*, 674, A1, doi: [10.1051/0004-6361/202243940](https://doi.org/10.1051/0004-6361/202243940)

Gao, X. 2018, *The Astronomical Journal*, 156, 121

Geller, A. M., Hurley, J. R., & Mathieu, R. D. 2013, *AJ*, 145, 8, doi: [10.1088/0004-6256/145/1/8](https://doi.org/10.1088/0004-6256/145/1/8)

Ginsburg, A., Sipőcz, B. M., Brasseur, C. E., et al. 2019, *AJ*, 157, 98, doi: [10.3847/1538-3881/aafc33](https://doi.org/10.3847/1538-3881/aafc33)

Goodwin, S. P. 2010, *Philosophical Transactions of the Royal Society A: Mathematical, Physical and Engineering Sciences*, 368, 851

Gratton, R. 2000, in *Astronomical Society of the Pacific Conference Series*, Vol. 198, *Stellar Clusters and Associations: Convection, Rotation, and Dynamos*, ed. R. Pallavicini, G. Micela, & S. Sciortino, 225

Groenewegen, M. A. T. 2023, *A&A*, 669, A4, doi: [10.1051/0004-6361/202244479](https://doi.org/10.1051/0004-6361/202244479)

Handler, G. 1999, *MNRAS*, 309, L19, doi: [10.1046/j.1365-8711.1999.03005.x](https://doi.org/10.1046/j.1365-8711.1999.03005.x)

Harris, C. R., Millman, K. J., van der Walt, S. J., et al. 2020, *Nature*, 585, 357, doi: [10.1038/s41586-020-2649-2](https://doi.org/10.1038/s41586-020-2649-2)

He, Z., Liu, X., Luo, Y., Wang, K., & Jiang, Q. 2022a, *The Astrophysical Journal Supplement Series*, 264, 8

He, Z., Li, C., Zhong, J., et al. 2022b, *The Astrophysical Journal Supplement Series*, 260, 8

Herbst, W., Herbst, D. K., Grossman, E. J., & Weinstein, D. 1994, *AJ*, 108, 1906, doi: [10.1086/117204](https://doi.org/10.1086/117204)

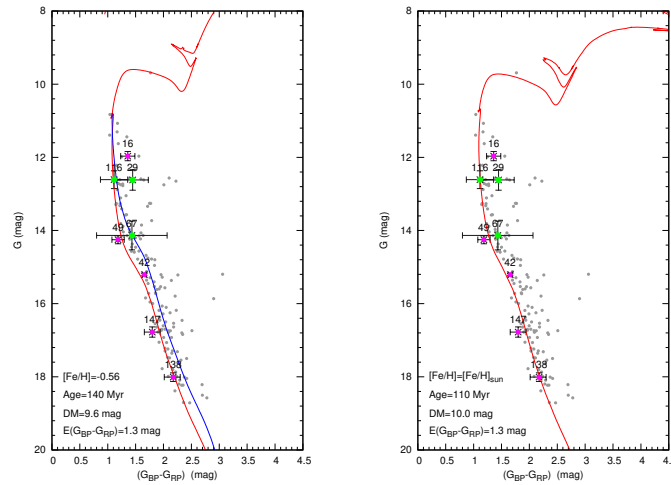


Figure 5. The observational G versus $(G_{BP} - G_{RP})$ CMDs of UPK 220 from GaiaDR3. The isochrones fitting is done via MIST considering two metallicities (left panel: $[Fe/H] = -0.56$, right panel: solar abundance). The member stars are described as grey dots. Magenta circles show eclipsing binary systems, whereas the green circles correspond to the single variables. The blue isochrone in the left panel represents the photometrical effects of the binary stars ($q = 1$) on the CMD.

- Herwig, F. 2000, *A&A*, 360, 952,
doi: [10.48550/arXiv.astro-ph/0007139](https://doi.org/10.48550/arXiv.astro-ph/0007139)
- Hunt, E. L., & Reffert, S. 2024, *A&A*, 686, A42,
doi: [10.1051/0004-6361/202348662](https://doi.org/10.1051/0004-6361/202348662)
- Hunt, E. L., & Reffert, S. 2024, *Astronomy & Astrophysics*, 686, A42
- Hunter, J. D. 2007, *Computing in Science & Engineering*, 9, 90, doi: [10.1109/MCSE.2007.55](https://doi.org/10.1109/MCSE.2007.55)
- Hurley, J., & Tout, C. A. 1998, *MNRAS*, 300, 977,
doi: [10.1046/j.1365-8711.1998.01981.x](https://doi.org/10.1046/j.1365-8711.1998.01981.x)
- Iglesias, C. A., & Rogers, F. J. 1993, *ApJ*, 412, 752,
doi: [10.1086/172958](https://doi.org/10.1086/172958)
- . 1996, *ApJ*, 464, 943, doi: [10.1086/177381](https://doi.org/10.1086/177381)
- Im, H., Kim, S. C., Kyeong, J., Park, H. S., & Lee, J. H. 2023, *The Astronomical Journal*, 165, 53
- Jenkins, J. M., Twicken, J. D., McCauliff, S., et al. 2016, in *Society of Photo-Optical Instrumentation Engineers (SPIE) Conference Series*, Vol. 9913, *Software and Cyberinfrastructure for Astronomy IV*, ed. G. Chiozzi & J. C. Guzman, 99133E, doi: [10.1117/12.2233418](https://doi.org/10.1117/12.2233418)
- Jiang, D. 2020, *Monthly Notices of the Royal Astronomical Society*, 492, 2731
- Joshi, Y. C., Joshi, S., Kumar, B., Mondal, S., & Balona, L. A. 2012, *MNRAS*, 419, 2379,
doi: [10.1111/j.1365-2966.2011.19890.x](https://doi.org/10.1111/j.1365-2966.2011.19890.x)
- Kharchenko, N., Piskunov, A., Hubrig, S., & Schöller, M. 2022, *Monthly Notices of the Royal Astronomical Society*, 515, 3094
- Kharchenko, N., Piskunov, A., Röser, S., Schilbach, E., & Scholz, R.-D. 2005, *Astronomy & Astrophysics*, 438, 1163
- Kharchenko, N., Piskunov, A., Schilbach, E., Röser, S., & Scholz, R.-D. 2013, *Astronomy & Astrophysics*, 558, A53
- Kim, S. C., Kyeong, J., Park, H. S., et al. 2017, *Journal of Korean Astronomical Society*, 50, 79,
doi: [10.5303/JKAS.2017.50.3.79](https://doi.org/10.5303/JKAS.2017.50.3.79)
- King, I. R. 1966, *The Astronomical Journal*, 71, 64,
doi: [10.1086/109857](https://doi.org/10.1086/109857)
- Krisciunas, K., & Patten, B. M. 1999, *Information Bulletin on Variable Stars*, 4705, 1
- Krumholz, M. R., McKee, C. F., & Bland-Hawthorn, J. 2019, *Annual Review of Astronomy and Astrophysics*, 57, 227
- Kunz, R., Fey, M., Jaeger, M., et al. 2002, *ApJ*, 567, 643,
doi: [10.1086/338384](https://doi.org/10.1086/338384)
- Lada, C. J., & Lada, E. A. 2003, *Annual Review of Astronomy and Astrophysics*, 41, 57
- Lata, S., Chen, W. P., Pandey, J. C., et al. 2023, *MNRAS*, 520, 1092, doi: [10.1093/mnras/stad013](https://doi.org/10.1093/mnras/stad013)
- Lightkurve Collaboration, Cardoso, J. V. d. M., Hedges, C., et al. 2018, *Lightkurve: Kepler and TESS time series analysis in Python*, *Astrophysics Source Code Library*.
<http://ascl.net/1812.013>
- Liu, L., & Pang, X. 2019, *The Astrophysical Journal Supplement Series*, 245, 32
- Liu, R., Shao, Z., & Li, L. 2025, arXiv e-prints, arXiv:2501.01617. <https://arxiv.org/abs/2501.01617>

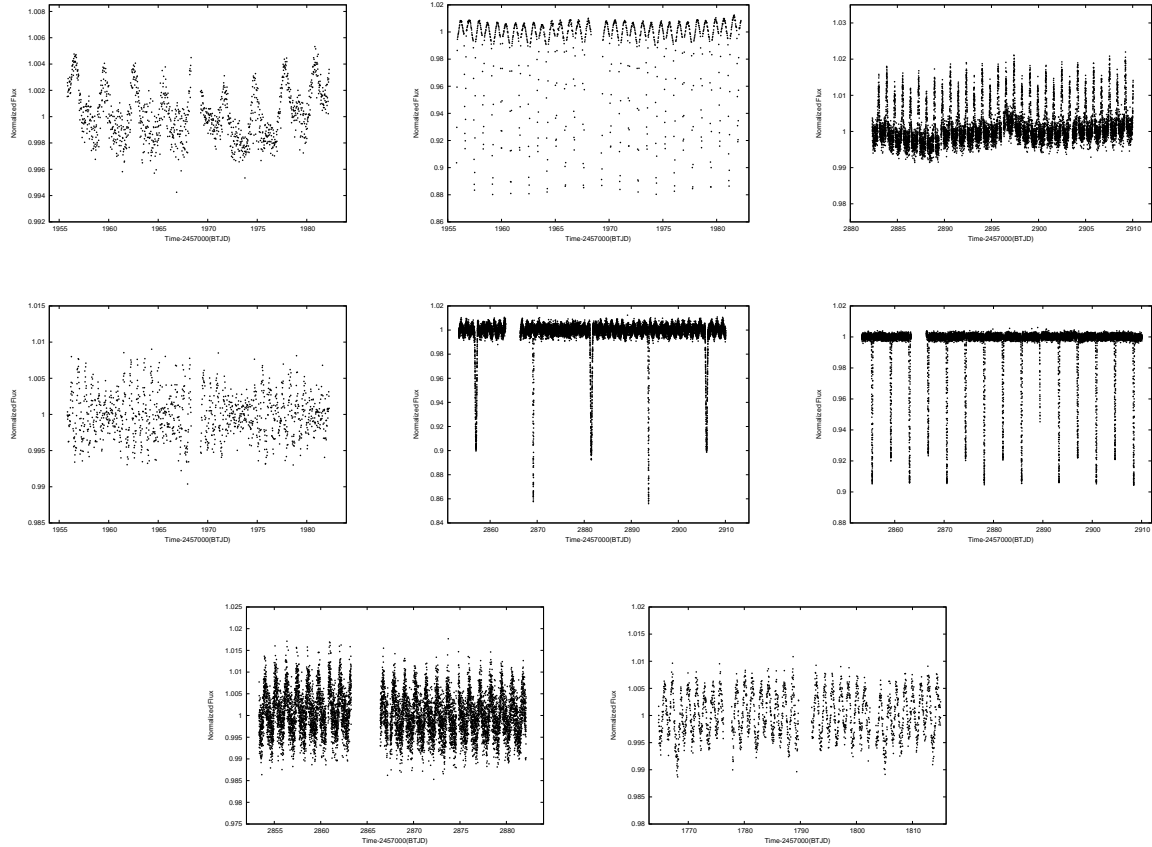


Figure 6. Normalized TESS light curves of variable member stars. First row: ID16 (Sector 24), ID29 (Sector 24) and ID42 (Sector 58). Second row: ID49 (Sector 24), ID67 (Sectors 57 and 58) and ID116 (Sectors 57 and 58). Third row: ID138 (Sector 57) and ID147 (Sectors 17 and 18).

Martin, D. V., Sethi, R., Armitage, T., et al. 2024, *MNRAS*, 528, 963, doi: [10.1093/mnras/stae015](https://doi.org/10.1093/mnras/stae015)

Mermilliod, J. 1981, *Astronomy and Astrophysics*, vol. 97, no. 2, Apr. 1981, p. 235-244., 97, 235

Molenda-Żakowicz, J., Kopacki, G., Steślicki, M., & Narwid, A. 2009, *AcA*, 59, 193, doi: [10.48550/arXiv.0907.0813](https://doi.org/10.48550/arXiv.0907.0813)

Mombarg, J. S. G., Van Reeth, T., Pedersen, M. G., et al. 2019, *Monthly Notices of the Royal Astronomical Society*, 485, 3248, doi: [10.1093/mnras/stz501](https://doi.org/10.1093/mnras/stz501)

Monteiro, H., Dias, W., Moitinho, A., et al. 2020, *Monthly Notices of the Royal Astronomical Society*, 499, 1874

Mowlavi, N., Barblan, F., Saesen, S., & Eyer, L. 2013, *Astronomy & Astrophysics*, 554, A108

Negueruela, I., & de Burgos, A. 2023, *Astronomy & Astrophysics*, 675, A19

Netopil, M., Oralhan, İ. A., Çakmak, H., Michel, R., & Karataş, Y. 2022, *MNRAS*, 509, 421, doi: [10.1093/mnras/stab2961](https://doi.org/10.1093/mnras/stab2961)

Owens, K. A., Freedman, W. L., Madore, B. F., & Lee, A. J. 2022, *ApJ*, 927, 8, doi: [10.3847/1538-4357/ac479e](https://doi.org/10.3847/1538-4357/ac479e)

Pace, G., Pasquini, L., & François, P. 2008, *A&A*, 489, 403, doi: [10.1051/0004-6361:200809969](https://doi.org/10.1051/0004-6361:200809969)

Paunzen, E., Heiter, U., Netopil, M., & Soubiran, C. 2010, *A&A*, 517, A32, doi: [10.1051/0004-6361/201014131](https://doi.org/10.1051/0004-6361/201014131)

Paunzen, E., Piecka, M., & Supikova, J. 2023, *Odessa Astronomical Publications*, 36, 77, doi: [10.18524/1810-4215.2023.36.291233](https://doi.org/10.18524/1810-4215.2023.36.291233)

Paxton, B., Bildsten, L., Dotter, A., et al. 2011, *ApJS*, 192, 3, doi: [10.1088/0067-0049/192/1/3](https://doi.org/10.1088/0067-0049/192/1/3)

Paxton, B., Marchant, P., Schwab, J., et al. 2015, *ApJS*, 220, 15, doi: [10.1088/0067-0049/220/1/15](https://doi.org/10.1088/0067-0049/220/1/15)

Paxton, B., Schwab, J., Bauer, E. B., et al. 2018, *ApJS*, 234, 34, doi: [10.3847/1538-4365/aaa5a8](https://doi.org/10.3847/1538-4365/aaa5a8)

Paxton, B., Smolec, R., Schwab, J., et al. 2019, *ApJS*, 243, 10, doi: [10.3847/1538-4365/ab2241](https://doi.org/10.3847/1538-4365/ab2241)

Pera, M. S., Perren, G. I., Moitinho, A., Navone, H. D., & Vazquez, R. A. 2021, *A&A*, 650, A109, doi: [10.1051/0004-6361/202040252](https://doi.org/10.1051/0004-6361/202040252)

Percy, J. R., Gryc, W. K., Wong, J. C. Y., & Herbst, W. 2006, *PASP*, 118, 1390, doi: [10.1086/508557](https://doi.org/10.1086/508557)

- Piatti, A. E., Claria, J. J., & Abadi, M. G. 1995, *AJ*, 110, 2813, doi: [10.1086/117731](https://doi.org/10.1086/117731)
- Piatti, A. E., Dias, W. S., & Sampedro, L. M. 2017, *Monthly Notices of the Royal Astronomical Society*, 466, 392
- Pietrzyński, G., Graczyk, D., Gallenne, A., et al. 2019, *Nature*, 567, 200
- Piskunov, A., Kharchenko, N., Röser, S., Schilbach, E., & Scholz, R.-D. 2006, *Astronomy & Astrophysics*, 445, 545
- Plachy, E., Pál, A., Bódi, A., et al. 2021, *ApJS*, 253, 11, doi: [10.3847/1538-4365/abd4e3](https://doi.org/10.3847/1538-4365/abd4e3)
- Poehnl, H., & Paunzen, E. 2010, *Astronomy & Astrophysics*, 514, A81
- Prusti, T., De Bruijne, J., Brown, A. G., et al. 2016, *Astronomy & astrophysics*, 595, A1
- Ricker, G. R., Winn, J. N., Vanderspek, R., et al. 2014, in *Society of Photo-Optical Instrumentation Engineers (SPIE) Conference Series*, Vol. 9143, *Space Telescopes and Instrumentation 2014: Optical, Infrared, and Millimeter Wave*, ed. J. Oschmann, Jacobus M., M. Clampin, G. G. Fazio, & H. A. MacEwen, 914320, doi: [10.1117/12.2063489](https://doi.org/10.1117/12.2063489)
- Ricker, G. R., Winn, J. N., Vanderspek, R., et al. 2015, *Journal of Astronomical Telescopes, Instruments, and Systems*, 1, 014003, doi: [10.1117/1.JATIS.1.1.014003](https://doi.org/10.1117/1.JATIS.1.1.014003)
- Santos, N. C., Lovis, C., Pace, G., Melendez, J., & Naef, D. 2009, *A&A*, 493, 309, doi: [10.1051/0004-6361:200811093](https://doi.org/10.1051/0004-6361:200811093)
- Sariya, D. P., Jiang, G., Bisht, D., Yadav, R., & Rangwal, G. 2023, *New Astronomy*, 98, 101938
- Schuler, S. C., King, J. R., Fischer, D. A., Soderblom, D. R., & Jones, B. F. 2003, *AJ*, 125, 2085, doi: [10.1086/373927](https://doi.org/10.1086/373927)
- Shen, D.-X., Zhang, Y., Li, C.-Y., et al. 2021, *Research in Astronomy and Astrophysics*, 21, 124
- Sikora, J., David-Uraz, A., Chowdhury, S., et al. 2019, *MNRAS*, 487, 4695, doi: [10.1093/mnras/stz1581](https://doi.org/10.1093/mnras/stz1581)
- Sim, G., Lee, S. H., Ann, H. B., & Kim, S. 2019, arXiv preprint arXiv:1907.06872
- Sim, G., Lee, S. H., Ann, H. B., & Kim, S. 2019, *Journal of Korean Astronomical Society*, 52, 145, doi: [10.5303/JKAS.2019.52.5.145](https://doi.org/10.5303/JKAS.2019.52.5.145)
- Soubiran, C., Cantat-Gaudin, T., Romero-Gómez, M., et al. 2018, *Astronomy & Astrophysics*, 619, A155
- Southworth, J., Maxted, P. F. L., & Smalley, B. 2004, *MNRAS*, 351, 1277, doi: [10.1111/j.1365-2966.2004.07871.x](https://doi.org/10.1111/j.1365-2966.2004.07871.x)
- Stassun, K. G., Oelkers, R. J., Paegert, M., et al. 2019, *AJ*, 158, 138, doi: [10.3847/1538-3881/ab3467](https://doi.org/10.3847/1538-3881/ab3467)
- Sun, Q., Wang, S. X., Gan, T., & Mann, A. W. 2022, *Research in Astronomy and Astrophysics*, 22, 075008
- Tadross, A. L. 2003, *NewA*, 8, 737, doi: [10.1016/S1384-1076\(03\)00062-9](https://doi.org/10.1016/S1384-1076(03)00062-9)
- Takata, M., Ouazzani, R. M., Saio, H., et al. 2020, *A&A*, 635, A106, doi: [10.1051/0004-6361/201936297](https://doi.org/10.1051/0004-6361/201936297)
- Tarricq, Y., Soubiran, C., Casamiquela, L., et al. 2022, *Astronomy & Astrophysics*, 659, A59
- . 2021, *Astronomy & Astrophysics*, 647, A19
- Torres, G., Latham, D. W., & Quinn, S. N. 2021, *ApJ*, 921, 117, doi: [10.3847/1538-4357/ac1585](https://doi.org/10.3847/1538-4357/ac1585)
- Uribe, A., Barrera, R., et al. 2002, *Revista Mexicana de Astronomía y Astrofísica*, 14, 33
- Vines, J. I., & Jenkins, J. S. 2022, *Monthly Notices of the Royal Astronomical Society*, 513, 2719, doi: [10.1093/mnras/stac956](https://doi.org/10.1093/mnras/stac956)
- Wang, H., Zhang, Y., Zeng, X., et al. 2022a, *The Astronomical Journal*, 164, 40
- Wang, L., Tanikawa, A., & Fujii, M. S. 2022b, *Monthly Notices of the Royal Astronomical Society*, 509, 4713
- Xin, Y., Zhang, X.-B., & Deng, L.-C. 2002, *Chinese Journal of Astronomy and Astrophysics*, 2, 481
- Yadav, R., Glushkhova, E., Sariya, D. P., et al. 2011, *Monthly Notices of the Royal Astronomical Society*, 414, 652
- Yalyaliev, L., Chemel, A., Carraro, G., & Glushkova, E. 2024, *AJ*, 167, 100, doi: [10.3847/1538-3881/ad1ff0](https://doi.org/10.3847/1538-3881/ad1ff0)
- Yang, W., Bi, S., Meng, X., & Liu, Z. 2013, *ApJ*, 776, 112, doi: [10.1088/0004-637X/776/2/112](https://doi.org/10.1088/0004-637X/776/2/112)
- Zhuo, J., Deng, L.-C., Wang, K., et al. 2021, *Research in Astronomy and Astrophysics*, 21, 227

APPENDIX

A. SED PHOTOMETRIC DATA

The SED fitting performed using Bayesian Model Averaging to obtain the best-fitted model parameters. To fit each SED of the variable member stars, we collected *2MASS* (J,H and K_s), *Gaia DR3* (G, G_{BP} , and G_{RP}), *Johnson* (U, B, V, R, and I), *PS1* (g,i, r, y, and z), *SDSS* (u, g, r, and i), *TESS* (Tmag), and *WISE* (W1, W2, W3 and W4) photometric data. Unfortunately, we were unable to obtain all the photometric data for each star. The data used in the SED fitting are listed in Table 8.

Table 8. The collected photometric data with their errors from various catalogs of the variable member stars for SED fitting.

Survey/Filter	ID16	ID29	ID42	ID49	ID67	ID116	ID138	ID147	ID167
2MASS-H	9.644 ± 0.029	10.322 ± 0.032	12.359 ± 0.031	12.177 ± 0.030	11.327 ± 0.035	10.838 ± 0.028	14.433 ± 0.048	13.784 ± 0.046	9.558 ± 0.026
2MASS-J	9.959 ± 0.023	10.595 ± 0.024	12.827 ± 0.025	12.513 ± 0.023	11.670 ± 0.026	11.055 ± 0.022	15.221 ± 0.052	14.399 ± 0.032	10.011 ± 0.023
2MASS-K _s	9.494 ± 0.024	10.126 ± 0.021	12.255 ± 0.026	12.062 ± 0.027	11.164 ± 0.024	10.691 ± 0.023	14.138 ± 0.079	13.600 ± 0.044	9.337 ± 0.022
GaiaDR3-G	11.976 ± 0.002	12.636 ± 0.001	15.226 ± 0.003	14.164 ± 0.001	14.148 ± 0.001	12.619 ± 0.002	18.043 ± 0.002	16.803 ± 0.001	12.667 ± 0.001
GaiaDR3-G _{BP}	12.704 ± 0.001	13.418 ± 0.005	16.203 ± 0.004	14.737 ± 0.002	14.791 ± 0.019	13.153 ± 0.001	19.313 ± 0.041	17.741 ± 0.006	13.823 ± 0.004
GaiaDR3-G _{RP}	11.134 ± 0.001	11.760 ± 0.003	14.238 ± 0.001	13.442 ± 0.001	13.089 ± 0.027	11.928 ± 0.001	16.921 ± 0.005	15.825 ± 0.003	11.593 ± 0.003
Johnson-B	-	15.539 ± 0.210	-	-	-	17.143 ± 0.305	-	-	-
Johnson-V	-	14.460 ± 0.098	-	-	-	16.329 ± 0.021	-	-	-
PS1-g	-	-	16.554 ± 0.004	14.859 ± 0.002	14.911 ± 0.016	12.996	19.907 ± 0.015	18.091 ± 0.007	14.249 ± 0.003
PS1-i	-	-	14.677 ± 0.003	13.834 ± 0.005	13.142	12.307	17.395 ± 0.004	16.256 ± 0.003	12.024
PS1-r	-	-	15.359 ± 0.003	14.211 ± 0.002	14.091 ± 0.036	12.553	18.317 ± 0.005	16.898 ± 0.008	12.753
PS1-y	-	-	14.005 ± 0.004	13.467 ± 0.003	13.293 ± 0.027	11.951	16.525 ± 0.006	15.607 ± 0.004	11.329
PS1-z	-	-	14.286 ± 0.002	13.632 ± 0.002	12.869	12.093	16.882 ± 0.003	15.888 ± 0.003	11.475
SDSS-g	-	14.958 ± 0.156	-	-	16.932 ± 0.289	17.371 ± 0.083	-	-	-
SDSS-r	-	14.068 ± 0.081	-	-	15.606 ± 0.022	15.971	-	-	-
SDSS-i	-	13.571 ± 0.079	-	-	15.282 ± 0.033	15.123	-	-	-
TESS	11.212 ± 0.051	11.788 ± 0.023	14.219 ± 0.021	13.503 ± 0.045	13.335 ± 0.007	12.012 ± 0.037	16.830 ± 0.151	15.821 ± 0.0381	11.527 ± 0.051
WISE-W1	9.253 ± 0.021	10.020 ± 0.022	12.064 ± 0.024	-	-	10.577 ± 0.023	-	-	9.168 ± 0.023
WISE-W2	9.263 ± 0.019	9.998 ± 0.019	12.039 ± 0.022	-	-	10.575 ± 0.021	-	-	9.127 ± 0.021